Applied Catalysis B: Environment and Energy 345 (2024) 123696

Contents lists available at ScienceDirect

Applied Catalysis B: Environment and Energy

journal homepage: www.elsevier.com/locate/apcatb

One-step synthesis of sludge-derived MnO_x catalysts for highly efficient removal of gaseous ozone from industrial flue gas

Lyumeng Ye [a,c,d], Wenjing Dai [b], Peng Lu [a,c,d], Jianhang Huang [a,c,d], Xianhui Yan [a,c,d], Changcheng Sun [a,c,d], Kuang He [a], Mingyang Zhang [a], Haibao Huang [b,*]

[a] South China Institute of Environmental Sciences, Ministry of Ecology and Environment, Guangzhou 510655, China
[b] School of Environmental Science and Engineering, Sun Yat-sen University, Guangzhou 510275, China
[c] Guangdong Province Engineering Laboratory for Air Pollution Control, Guangzhou 510655, China
[d] Guangdong Provincial Key Laboratory of Water and Air Pollution Control, Guangzhou 510655, China

ARTICLE INFO

Keywords:
Sludge-derived catalysts
β-MnOOH
Ozone pollution
Industrial flue gas
Catalytic decomposition

ABSTRACT

A series of sludge-derived MnO_x catalysts were successfully obtained by a one-step sludge disintegration process using $KMnO_4$. The obtained S-MnO_x-1.2 catalyst exhibited excellent activity and superior water resistance under industrial flue gas conditions (5 vol% H_2O, 40–80 ℃, 300,000–600,000 mL/(g·h) of GHSV). β-MnOOH was the predominant component generated on the sludge surface by a redox reaction between $KMnO_4$ and organic matter. The superior ozone decomposition performance was mainly ascribed to its large surface area, plentiful oxygen vacancies and interlayer hydroxyl groups. There were two types of surface oxygen vacancies, denoted as ozone-friendly and hydrophilic oxygen vacancies, participated in the ozone elimination process. Surface hydroxyl groups physically adsorbed abundant water molecules and hindered the chemisorption of water on ozone-friendly oxygen vacancies, thereby increasing the water resistance of the catalyst. The present work produced a potential catalyst in favor of ozone elimination, and promoted the high value-added utilization of waste sludge.

1. Introduction

Tropospheric ozone (O_3), as a typical air pollutant and a greenhouse gas, is harmful to human health and vegetation [1]. The Chinese government proposes to limit the O_3 concentration to 100 μg/m^3 (maximum daily 8-hour average, MDA8) in the ambient air quality standards (GB3095–2012). The World Health Organization (WHO) also issued the Global Air Quality Guideline value in 2021 (AQG 2021) and set the average exposure O_3 concentration at 60 μg/m^3 . It is generally accepted that ambient O_3 is a secondary pollutant, formed by the reaction between nitrogen oxides (NO_x) and volatile organic compounds (VOCs) through a series of photochemical processes [2,3]. Numerous efforts have been carried out for the control of NO_x and VOCs to effectively reduce O_3 pollution levels [4,5]. However, it is noteworthy that industrial flue gases, such as those from metallurgical, glass, and ceramic industries, etc., can directly release O_3 as a primary pollutant. Recently, our research groups monitored the O_3 concentration extracted from industrial flue gas, and found it to be in the range of 150 to 130000 μg/m^3 (Table S1). The temperature of these industrial flue gases was simultaneously monitored to be in the range of 40 to 120 °C. High levels of gaseous ozone emissions from the industrial flue gases have significantly contributed to elevated ambient O_3 levels above acceptable standards [6]. This problem has raised great concerns among the public and governments. Therefore, it is imperative to reduce gaseous ozone emission from industrial flue gases to minimize its negative impact on the environment.

Catalytic decomposition stands as the most promising approach for O_3 removal. Noble metal catalysts (Ag, Pt, Pd) and transition metal oxide catalysts (Ni, Fe, Co, Mn) have decent performance for O_3 decomposition [7]. Among these catalysts, Mn oxides have great application prospects in O_3 catalytic decomposition due to their economic, non-toxic, and especially on account of their excellent catalytic activity. It is well known that ozone decomposition process involves redox process and oxygen migration. Mn oxides can provide a renewable redox reaction of Mn^{3+}/Mn^{4+}, and enable superior oxygen mobility in the oxide lattice [8]. As a result, MnO_x are the most common active components for ozone elimination, and MnO_x-based catalysts have been widely used in practical applications. Supported MnO_x is one of the

---

* Corresponding author.
E-mail address: seabao8@gmail.com (H. Huang).

https://doi.org/10.1016/j.apcatb.2024.123696
Received 25 October 2023; Received in revised form 18 December 2023; Accepted 1 January 2024

feasible catalysts for O_3 decomposition. Different types of supports, including activated carbon (AC), CNTs, graphene, TiO_2, and Al_2O_3, can affect the specific surface area, the average Mn oxidation state, the concentration of oxygen vacancies, and the exposed crystal facets of the MnO_x catalysts [9–12].

Over the past decade, the utilization of waste-derived materials as catalyst supports has gained popularity [13,14]. Sludge is the semi-solid product left over from wastewater treatment, and its safe disposal is a pressing issue due to the explosive growth of waste sludge. Converting waste sludge into environmental catalysts is considered as a sustainable and non-harmful approach to both maximizing waste valorization and decreasing hazardous organic waste [15]. Potassium permanganate ($KMnO_4$) is used as a potent oxidant. It is widely employed to destroy sludge cells and flocs, oxidize organic matter, boost the sludge dewatering capacity, and ultimately promote the safe disposal of waste sludge [16,17]. During the $KMnO_4$-assisted sludge disintegration process, it is possible that $KMnO_4$ can act as a chemical modifier to incorporate Mn oxides onto the sludge surface and thus contribute to the synthesis of Mn oxide-doped catalysts. These catalysts may possess great potential in the catalytic removal of environmental pollutants. Inspired by the above discussions, we carried out a preliminary experiment and found that massive Mn oxides were generated on the sludge surface after a $KMnO_4$-assisted sludge disintegration process. It is highly interesting to note that these sludge-derived MnO_x catalysts could achieve outstanding ozone decomposition activity in the simulated industrial flue gas.

Thus, our study will comprehensively investigate the textural, physical and chemical properties of these sludge-derived MnO_x catalysts by X-ray fluorescence analysis (XRF), X-ray diffraction (XRD), N_2 adsorption-desorption, scanning electron microscopy (SEM), transmission electron microscopy (TEM), H_2 temperature programmed reduction (H_2-TPR), O_2 temperature programmed desorption (O_2-TPD), X-ray photoelectron spectroscopy (XPS), and 77 K low-temperature electron paramagnetic resonance (EPR). The possible reaction mechanism for ozone decomposition will be concluded with the aid of in situ DRIFT and H_2O-TPD. Such sludge-derived MnO_x catalysts serve as promising catalysts to control the industrial ozone pollution and are expected to provide a cost-effective and eco-friendly method for sludge valorization.

2. Experiment section

2.1. Catalyst synthesis

Sewage sludge after mechanical dewatering was collected from the JingXi wastewater treatment plant located in Guangzhou, China. The sludge-derived MnO_x catalysts were obtained by a redox reaction between $KMnO_4$ and sewage sludge (Fig. S1). In brief, a certain amount of $KMnO_4$ was first dissolved in 0.1 mol/L HCl to get solution A. Afterwards, 2 g sewage sludge was added into solution A. The resulting mixed solution was vigorously stirred in a water bath at 80 ℃ for 1 h. Subsequently, the mixture was centrifuged and repeatedly washed with deionized water until Cl species was undetectable by an $AgNO_3$ solution. Finally, the obtained solid was dried at 105 ℃ for 12 h. The catalysts were denoted as S-MnO_x-y, where y represented the added mass (g) of $KMnO_4$ ($y = 0$, 0.6, 1.2, 2.4). When $y = 0$, the sample was denoted as S.

2.2. Catalyst characterization

Ultimate analysis of the samples was performed by Elementar Analysensysteme GmbH. Proximate analysis was conducted by thermogravimetric analyzer (STA 449 F3 Jupiter®, NETZSCH). XRF ananlysis

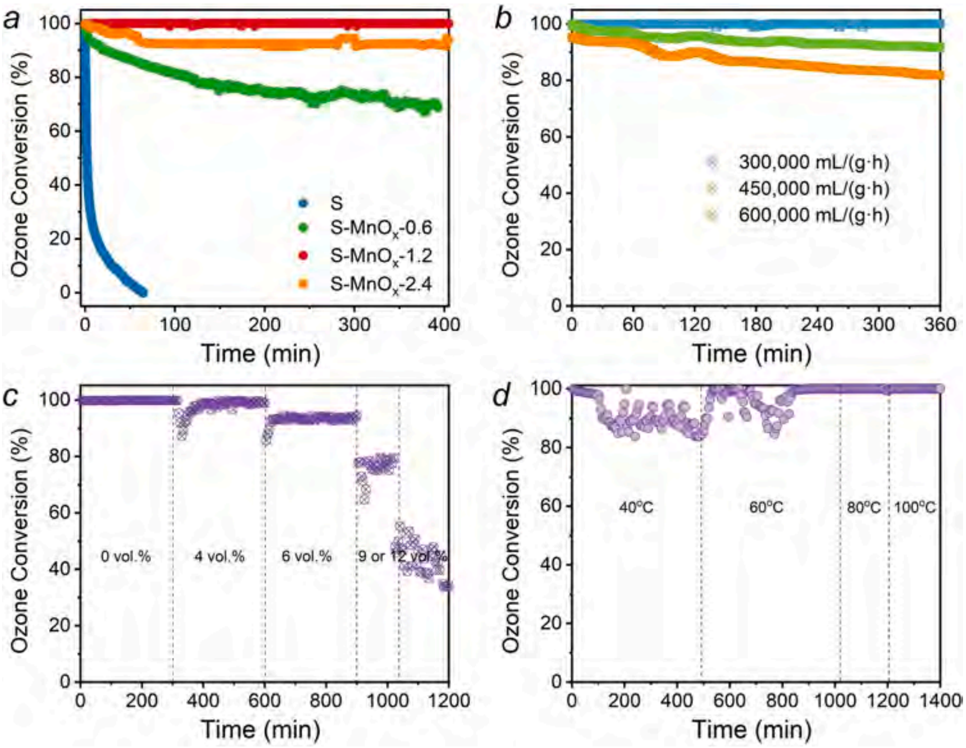

Fig. 1. (a) ozone conversion over S, S-MnO_x-0.6, S-MnO_x-1.2 and S-MnO_x-2.4. (Reaction condition: ozone concentration = 60 ppm, H_2O = 5 vol%, GHSV = 300,000 mL/(g·h), temperature = 60 ℃). (b) ozone conversion under different GHSV over S-MnO_x-1.2 (Reaction condition: ozone concentration = 60 ppm, H_2O = 5 vol%, temperature = 60 ℃). (c) different water vapor gradient experiment over S-MnO_x-1.2 (Reaction condition: ozone concentration = 60 ppm, temperature = 60 ℃, GHSV = 300,000 mL/(g·h). The catalyst was not replaced and the water vapor was gradually increased from 4 to 12 vol% without stopping). (d) different temperature gradient experiment over S-MnO_x-1.2 (Reaction condition: ozone concentration = 60 ppm, H_2O = 5 vol%, GHSV = 300,000 mL/(g·h). The catalyst was not replaced and the temperature was gradually increased from 40 to 100 ℃ without stopping).

(Malvern Panalytical Axios FAST) was used to characterize the composition of the samples.

The powder XRD pattern was recorded using an X-ray diffractometer equipped with Cu Kα radiation (model D/max RA, Rigaku Co., Japan). A chemisorption analyzer (Micromeritics ASAP 2020, USA) was used to obtain the nitrogen adsorption-desorption isotherms and physical data for the catalysts. The surface area and pore size distribution were determined using the standard Brunauer–Emmett–Teller (BET) procedure and Barrett–Joyner–Halenda (BJH) model. The O, Mn and Ce binding energies were determined by a photoelectron spectroscopy (Thermo Scientific) with Al Kα X-ray radiation (1486.6 eV) operated at 150 W. Low-temperature EPR spectra were acquired on a Bruker EMX EPR spectrometer (Billerica, MA) at 77 K in a vacuum. The Raman spectra were obtained on a microscopic confocal Raman spectrometer (Horiba HR800, Jobin-Yvon, Inc., France) from 100–1000 cm^{-1}, with an excitation wavelength of 532 nm. The morphology of the catalysts was characterized by SEM (Quanta 400 FEG, FEI, America). HR-TEM images were taken with a JEM-2010 TEM (Japan) operated at 200 kV.

H_2-TPR, O_2-TPD and H_2O-TPD were all conducted on an AutoChemII 2920 instrument (Micromeritics, USA). Prior to the reduction reaction, ~50 mg of the sample was pretreated under a flow of highly purified He for 20 min at 200 °C and then cooled to 50 °C. The H_2-TPR experiments begin from 50 °C and heated to the target temperature (800 °C) at a heating rate of 10 °C/min under a flow of 10 vol% mixed H_2/Ar gas (50 cm^3 STP/min). Prior to passing through the detector, the exhaust gases were cooled to − 80 °C in a liquid nitrogen cooled isopropanol trap. The analyzer was calibrated with AgO. For O_2-TPD analysis, each sample (100 mg) was pretreated at 200 °C in a flow of He (30 mL/min) for 60 min. After cooling to room temperature, the gas was changed to O_2/Ar (30 mL/min), heating from 100 to 800 °C. For H_2O-TPD analysis, each sample (100 mg) was pretreated at 110 °C in a flow of Ar (30 mL/min) for 60 min. Programming was started at a rate of 10 °C/min from 50 to 900 °C under Ar flow. The effluent gases were determined by an on-line mass spectrometer (QGA, Hiden Analytical Ltd.). The signals at mass-to-charge (m/z) ratios of 18 (H_2O) were detected.

In situ DRIFTs experiments were conducted using a Bruker FT-IR spectrometer (VERTEX 70) equipped with an MCT detector. A DRIFTs cell (PIKE TECHNOLOGIES) with a ZnSe window was fitted into a heating cartridge. Prior to the measurement, the samples were preheated at 105 °C for 1 h under a 100 mL/min gas flow of N_2 gas and then cooled naturally. After pretreatment, the sample was cooled to the desired reaction temperature to collect the background. Then, the reactants were continuously introduced into the reaction chamber. The DRIFTs spectra were collected in 64 scans with a resolution of 4 cm^{-1}.

2.3. Activity measurements

The ozone decomposition tests were carried out in a fixed-bed quartz reactor (i.d. = 8 mm) using 0.06 g sample (40 –60 meshes). The gas mixture was composed of 60 ppm O_3, 5 vol% H_2O and balanced with N_2 (Fig. S2). The flow rate was 300 mL/min, and the gas hourly space velocity (GHSV) was 300,000 mL/(g·h). O_3 was produced by an O_3 generator (UV-M2, Tonglin Technologies, China) and monitored using an O_3 detector (model 106-L, 2B Technologies, USA). The ozone conversion was calculated by the following equation:

$$O_3 \text{ conversion } (\%) = \frac{C_{in} - C_{out}}{C_{in}} \times 100\%$$

where C_{in} (ppm) and C_{out} (ppm) were the inlet and outlet concentration of ozone, respectively.

Table 1
Proximate analyses, ultimate analyses and XRF results of the as-prepared sludge-derived catalysts.

Catalysts	S	S-MnO_x-0.6	S-MnO_x-1.2	S-MnO_x-2.4
Proximate analysis (as received, wt%)				
Ash	45.25	59.33	71.28	78.07
Volatiles	42.22	33.34	22	14.59
Moisture	6.09	5.35	6.65	7.30
Fixed carbon[a]	6.44	1.98	0.07	0.04
Ultimate analysis (as received, wt%)				
C	21.91	12.55	5.63	2.70
H	1.31	0.78	0.63	0.52
N	3.32	1.60	0.63	0.30
S	0.15	0.085	0.065	0.038
O[a]	21.97	20.30	15.11	11.07
Chemical composition (wt%)				
Si	25.06	23.86	22.02	18.82
Al	25.74	23.75	21.42	17.91
Mn	0.21	19.6	33.4	56.05
K	0.39	1.72	2.35	4.85
Ca	1.97	1.89	1.67	1.24
Mg	0.44	0.41	0.38	0.27
Na	0.06	0.05	0.06	0.05

[a] Difference value

3. Results and discussion

3.1. Ozone catalytic decomposition performance

The ozone removal efficiencies of different sludge-derived MnO_x catalysts (S-MnO_x-y) were evaluated under a condition of 5 vol% H_2O at 60 ℃, which was similar to that of industrial flue gas. As depicted in Fig. 1(a), the ozone removal efficiency of S-MnO_x-1.2 was stable at approximately 99% for nearly 7 h, surpassing that of S-MnO_x-0.6 (about 60%) and S-MnO_x-2.4 (around 92%). Although both S-MnO_x-1.2 and S-MnO_x-2.4 could achieve more than 90% of ozone conversion, the $KMnO_4$ addition in S-MnO_x-2.4 was twice that added in S-MnO_x-1.2. Based on the amount and price of raw materials, the cost of S-MnO_x-1.2 was calculated. Meanwhile, the cost of typical ozone decomposition catalysts reported in the literatures have been calculated in our previous work [12]. Compared with these costs, the S-MnO_x-1.2 catalyst possessed the advantages of low cost (~2.0$/kg). Most of the cost for S-MnO_x-1.2 was from $KMnO_4$, which was ~5.0$/kg provided by the suppliers, while waste sludge did not require any cost and could even receive subsidies from the Chinese government (0.07$/kg). Most importantly, S-MnO_x-1.2 catalysts were obtained directly from the $KMnO_4$-assisted sludge disintegration process. Waste sludge was directly converted into environmental catalysts, which both maximized the waste valorization and reduced the hazardous organic waste. Consequently, S-MnO_x-1.2 was an optimal catalyst that significantly reduced the application cost for ozone removal.

Ozone conversion could consistently exceeded 80% over a 6-hour operation under the GHSV of 300,000 mL/(g·h) to 600,000 mL/(g·h) over the S-MnO_x-1.2 catalyst, indicating that S-MnO_x-1.2 was less susceptible to GHSV changes (Fig. 1(b)). Water vapor and temperature gradient experiments were carried out on S-MnO_x-1.2. As the water vapor was gradually increased without stopping, the efficiency of ozone decomposition remained above 90% at water vapor ≤ 6 vol% (Fig. 1(c)). However, when the water vapor concentration reached more than 9 vol%, excess water vapor covered the surface of the catalyst and prevented O_3 from being adsorbed on the active sites, causing the ozone conversion to significantly drop to ~45% at 12 vol% water vapor [18,19]. Temperature remarkably promoted the ozone removal efficiency, with this enhancement becoming even more pronounced as the temperature continued to increase (Fig. 1(d)). The ozone decomposition efficiency could be maintained at more than 80% within the industrial flue gas temperature range of 40 to 80 ℃. The performance results confirmed that the S-MnO_x-1.2 catalyst has great application potential

Table 2
BET, H_2-TPR, O_2-TPD and XPS results of the catalysts.

Catalysts	BET		H_2-TPR			O_2-TPD	XPS		
	S_{BET} (m^2/g)	Pore size (nm)	Total H_2 consumption amount (μmol/g)	α Peak Temperature (°C)	α peak H_2 consumption amount (μmol/g)	Desorption temperature (°C)	$(Mn^{2+}+Mn^{3+})/Mn^{4+}$	O_{ads}/O_{latt}	AOS
S	5.90	19.15	258.31	471	25.78	360	/	0	/
S-MnO_x-0.6	65.51	7.35	618.48	414	304.50	359	1.60	4.30	3.17
S-MnO_x-1.2	109.48	5.85	941.90	383	795.29	355	1.93	10.07	3.00
S-MnO_x-2.4	57.08	5.94	1407.15	392	529.57	382	1.11	4.78	3.24

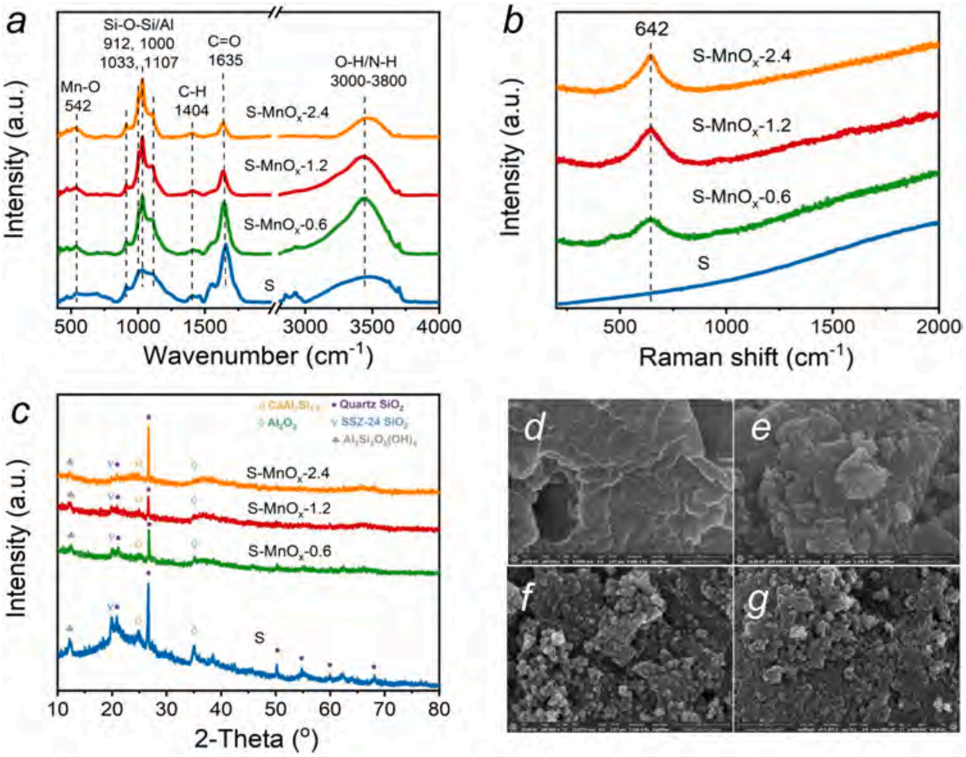

Fig. 2. (a) FTIR spectra, (b) Raman spectra, (c) XRD patterns and SEM images of (d) S, (e) S-MnO_x-0.6, (f) S-MnO_x-1.2 and (g) S-MnO_x-2.4.

for the catalytic removal of ozone from industrial flue gases.

3.2. Characterizations of sludge-derived MnO_x catalysts

As shown in Table 1, the contents of volatiles, fixed carbon and C, H, O, N, S significantly decreased with an increase in the amount of $KMnO_4$, suggesting that the sludge organic matter was disintegrated. During the $KMnO_4$-assisted sludge disintegration process, the extracellular polymeric substances (EPS) and refractory organic matter within the sludge flocs and cells were directly oxidized into dissolved organic matter. In some cases, these substances were even oxidized into carbonate and subsequently washed away. As a result, there was a loss of volatiles, fixed carbon as well as C, H, O, N, S [16,17]. The XRF results revealed that the pure sludge (S) was composed primarily of SiO_2 and Al_2O_3. After $KMnO_4$ conditioning, the catalysts displayed a significant increase in Mn and K contents, while other elements exhibited insignificant changes.

N_2 adsorption-desorption experiment was carried out. All obtained samples displayed a type IV isotherm (IUPAC classification) and pore size exceeding 2 nm, confirming that they were all mesoporous structures (Fig. S4 and Table 2). In comparison to the pure sludge (S), the BET surface area (S_{BET}) showed a significant increase after $KMnO_4$ conditioning. Among the samples, S-MnO_x-1.2 exhibited the highest S_{BET} value, indicating that more active sites were likely exposed on the catalyst surface. This, in turn, enhanced the catalytic performance of ozone decomposition [20].

Surface functional groups were analyzed by FTIR (Fig. 2(a)). A medium intensity peak at around 542 cm^{-1} was attributed to the Mn–O lattice vibrations of the $[MnO_6]$ octahedra group [21]. A broad band appeared at around 3000–3800 cm^{-1} corresponding to the vibration of O-H/N-H bonds [22,23]. The stretching of C=O and C-H bonds was observed at 1634 and 1404 cm^{-1}, respectively. The intensities of C=O and C-H peaks significantly decreased with the addition of $KMnO_4$, suggesting the disintegration of organic matter contained in the waste sludge. The Raman spectra displayed an obvious peak at 642 cm^{-1} of the as-prepared sludge-derived catalysts (Fig. 2(b)), which originated from the A1g symmetric "breathing" of Mn–O in the $[MnO_6]$ octahedra group [24]. The powder XRD patterns of sludge indicated the presence of SiO_2, Al_2O_3, and some compounds with Si and Al elements. In addition, S-MnO_x-*y* catalysts did not yield distinct characteristic peaks for MnO_x, suggesting that Mn oxides might be highly dispersed in the sludge (Fig. 2 (c) and Table S3).

The morphology and structure were detected by SEM and TEM. The

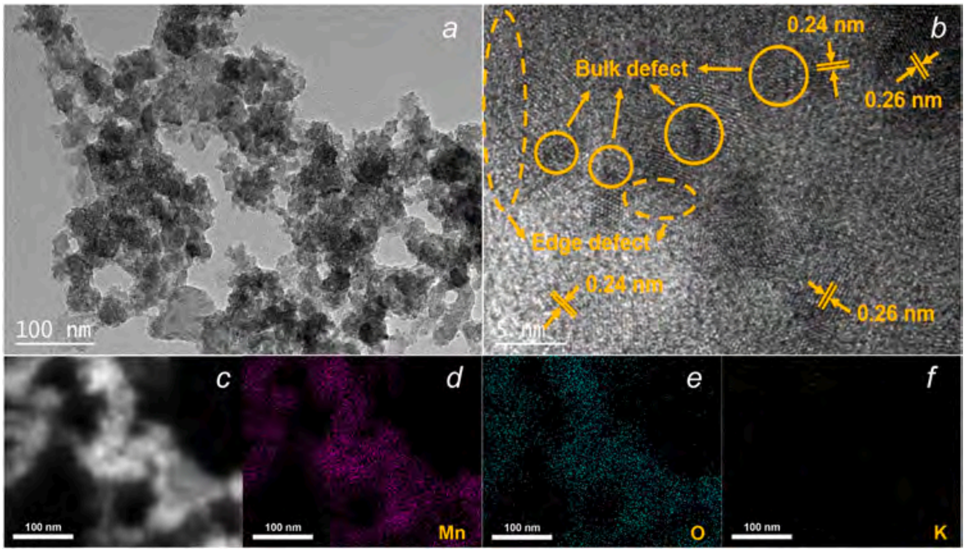

Fig. 3. TEM image, HRTEM image and corresponding EDX Mn, O, K element mapping of S-MnO_x-1.2.

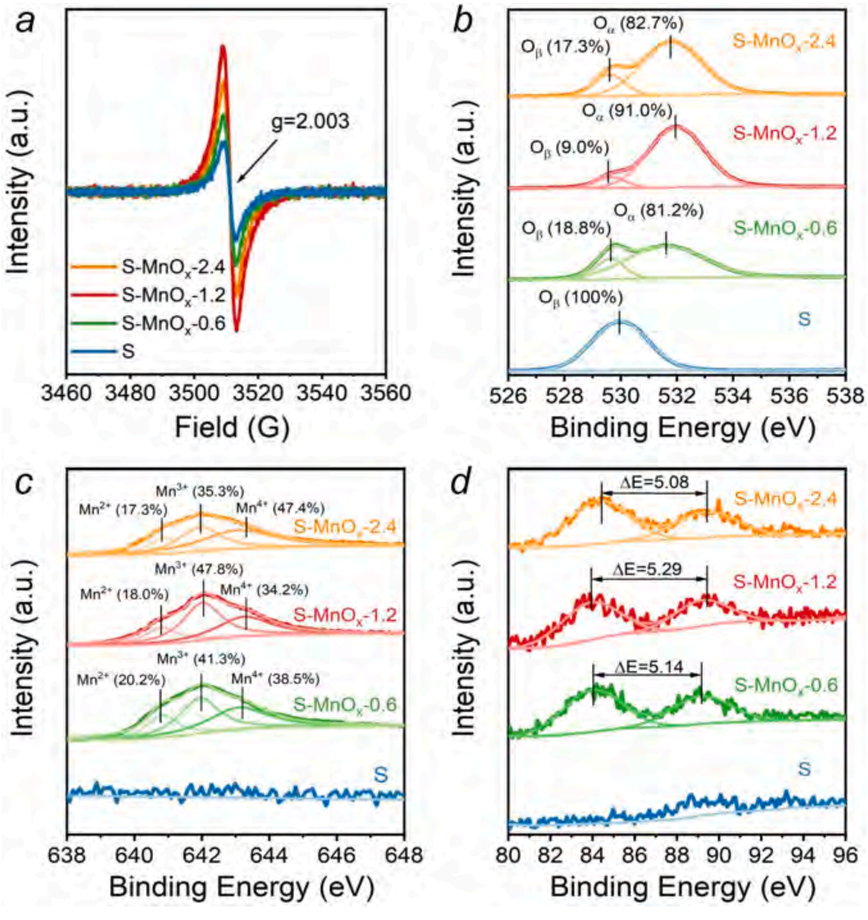

Fig. 4. (a) Low-temperature (77 K) EPR spectra, XPS spectra of (b) O 1 *s*, (c) Mn 2*p* and (d) Mn 3 *s*.

surface of pure sludge (S) was found to be highly rough (Fig. 2(d)). After the sludge was treated with $KMnO_4$, plenty of irregular nanoparticles were dispersed on the sludge surface (Fig. 2(e-g)). Taking S-MnO_x-1.2 as an illustration, the SEM image showed that the particle sizes of irregular nanoparticles were in the range of 10 to 60 nm (Fig. S5). Meanwhile, the TEM image revealed that the S-MnO_x-1.2 structure appeared loose (Fig. 3(a)). Numerous edge and bulk defects were clearly observed in the HRTEM images (Fig. 3(b)), which were generally considered to be active sites for the adsorption and decomposition of ozone molecules [25,26].

Low temperature EPR was utilized to confirm the presence and quantify the oxygen vacancies (Vo). Each sample exhibited a symmetric EPR signal peak at $g = 2.003$ (Fig. 4(a)), indicating the presence of unpaired electrons trapped by Vo [12,27]. The signal intensity directly correlated with the concentration of oxygen vacancies [28]. S-MnO_x-1.2

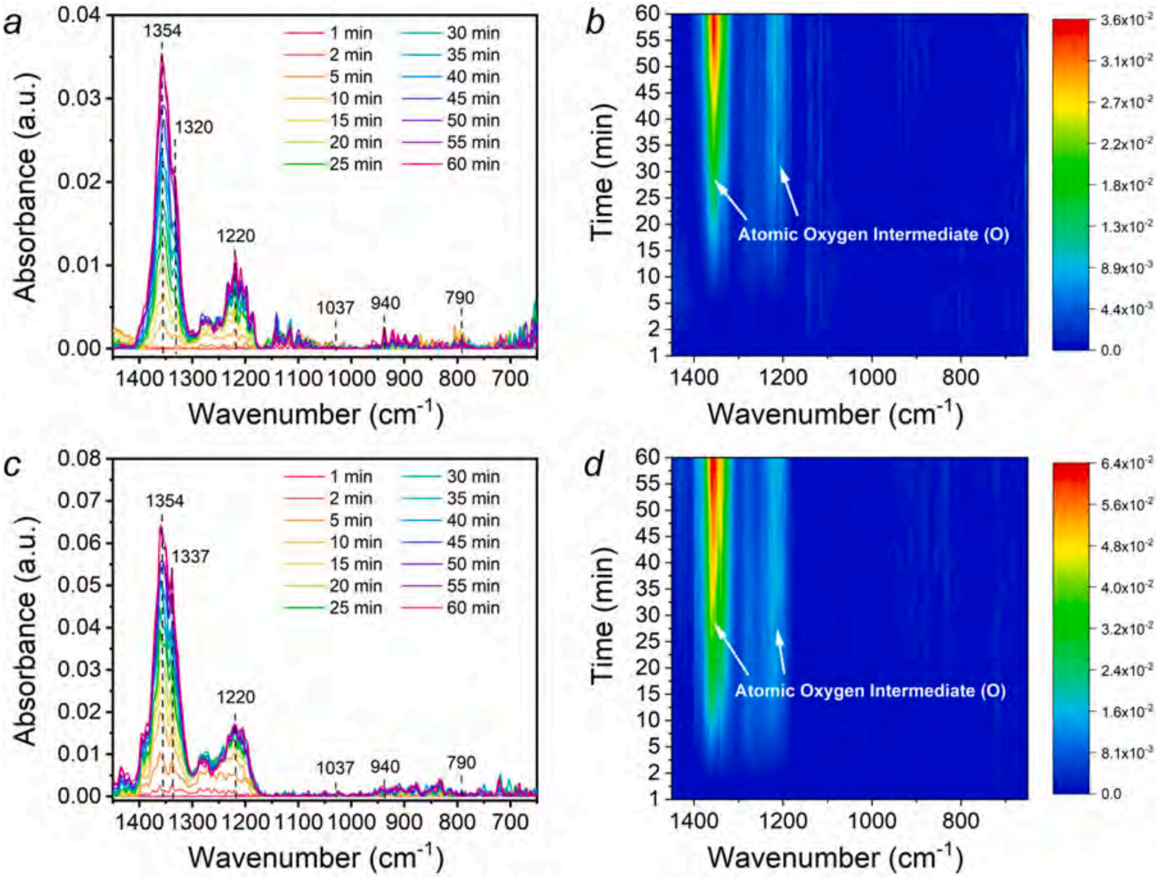

Fig. 5. In situ DRIFTs spectra of ozone decomposition process over S-MnO_x-1.2 catalyst, (a, b) under dry condition, and (c, d) under wet condition.

had a higher Vo concentration than the other samples. Chemical states were studied using XPS measurements. The O 1 *s* spectra were analyzed and identified as two distinct peaks with binding energies at approximately 529.5–529.7 eV and 531.5–531.9 eV. These peaks corresponded to lattice oxygen (O_β) and surface adsorbed oxygen (O_α) with low coordination, respectively (Fig. 4(b)). Table 2 clearly illustrated that S-MnO_x-1.2 owned the highest content of surface adsorbed oxygen. The content of surface adsorbed oxygen can be associated with the concentration of oxygen vacancies, since oxygen molecules tend to adsorb on the oxygen vacancies of metal oxide materials [25,29].

The valence state of Mn ions was characterized by analyzing the Mn $2p_{3/2}$ XPS spectra (Fig. 4(c)). The binding energies of the Mn^{2+}, Mn^{3+} and Mn^{4+} peaks were located at 640.5–641.5, 641.6–642.6 eV and 643.5–643.8 eV, respectively. The S-MnO_x-1.2 catalyst had the highest (Mn^{2+}+Mn^{3+})/Mn^{4+} ratio (1.93). The splitting energies (ΔE) derived from the Mn 3 *s* fell within the range of 5.08–5.29 eV (Fig. 4(d)), and the average oxidation state (AOS) was calculated using the formula AOS $= 8.956–1.126\Delta E$ [30]. The AOS values were 3.17 for S-MnO_x-0.6, 3.00 for S-MnO_x-1.2, and 3.24 for S-MnO_x-2.4 (Table 2), suggesting that S-MnO_x-1.2 was predominantly composed of Mn^{3+}. The Mn^{3+} content could be also considered as an indicator of the oxygen vacancy concentration in manganese oxides, based on the process $[–Mn^{4+}–O^{2-}–Mn^{4+}–] \rightarrow [–Mn^{3+}–Vo–Mn^{3+}–] + 1/2\ O_2$. The low-valence Mn on the surface facilitated the dissociation and activation of nearby oxygen atoms. Oxygen vacancies were subsequently generated to balance the charge because of the downshift of Mn^{4+} [31,32]. Abundant oxygen vacancies have been supposed to play an important role in ozone decomposition [20,33]. The XPS results of O 1 *s*, Mn 2*p* and Mn 3 *s* all confirmed that S-MnO_x-1.2 possessed a higher concentration of oxygen vacancies thus having the best ozone decomposition performance.

It is worth noting that the Mn AOS value of S-MnO_x-1.2 was +3.00. According to previous researches [34–36], the crystal phase of the Mn AOS value of +2.9 to +3.1 could be considered as feitknechtite β-MnOOH. From the HRTEM image in Fig. 3(b), lattice fringes of 0.26 nm and 0.24 nm could be identified on S-MnO_x-1.2, which were assigned to the (311) and (312) planes of β-MnOOH, respectively. The possible formation pathway of feitknechtite β-MnOOH on the sludge surface could be deduced as follows:

Organic Matters + $MnO_4^- + H^+ \rightarrow Mn^{2+} + H_2O + CO_3^{2-}$	Reaction 1
MnO_4^- + Organic Matters + $H_2O \rightarrow$ δ-$MnO_2 + CO_3^{2-} + HCO_3^-$	Reaction 2
$2MnO_4^- + 3Mn^{2+} + 2\ H_2O \rightarrow 5$δ-$MnO_2 + 4\ H^+$	Reaction 3
Mn^{2+} + δ-$MnO_2 + H_2O \rightarrow$ β-MnOOH $+ 2\ H^+$	Reaction 4
$MnO_4^- + 4Mn^{2+} + 6\ H_2O \rightarrow 5$β-MnOOH $+ 7\ H^+$	Reaction 5

During the $KMnO_4$-assisted sludge disintegration process, $KMnO_4$, as a strong oxidant, reacted with organic matter to produce Mn^{2+} and birnessite δ-MnO_2 (Reactions 1–3). On the one hand, it is possible that Mn^{2+} could facilitate the reductive transformation of birnessite δ-MnO_2 to feitknechtite β-MnOOH through interfacial electron transfer, as demonstrated in Reaction 4. On the other hand, the MnO_4^- may not be sufficient to oxidize Mn^{2+} into birnessite δ-MnO_2 (Reaction 3); instead, feitknechtite β-MnOOH intermediates would be generated (Reaction 5) [34,37]. As reported in the literatures, birnessite δ-MnO_2 displayed a 2D layered structure with excess K^+ within its mezzanines [32,34]. However, it can be seen from the EDX mapping that the Mn and O elements were in high dispersion degree, while the K element was less dispersed (Fig. 3(d, e, f)), implying again that feitknechtite β-MnOOH was the main MnO_x component of the S-MnO_x-1.2 sample instead of the birnessite δ-MnO_2.

There were two well-defined peaks in the H_2-TPR profiles (Fig. S6). The former peak (α) at 300–420 ℃ was assigned to the reduction process

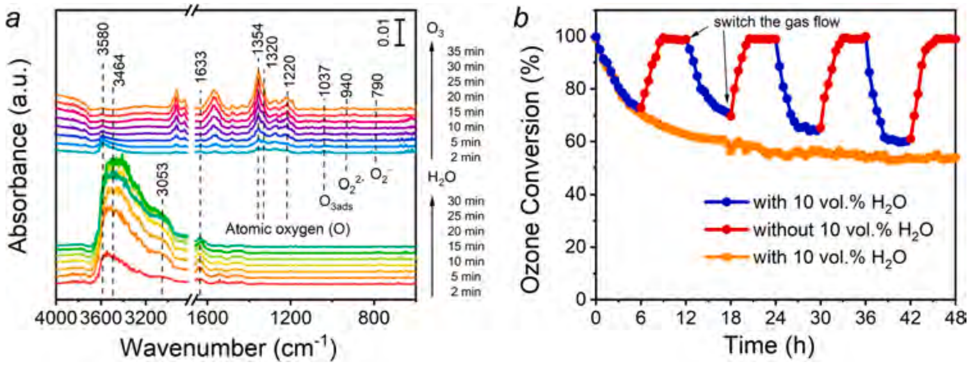

Fig. 6. (a) In situ DRIFTs spectra of gaseous O_3 passed over the water pre-exposed S-MnO_x-1.2 catalyst (Reaction condition: 10 vol% of water vapor introduced in 0–30 min, and switched to 60 ppm ozone without water vapor addition for the next 35–70 min, temperature = 60 ℃), and (b) ozone conversion in alternating humid and dry condition. Reaction condition: ozone concentration = 60 ppm, H_2O = 10 vol% (when used), GHSV = 300,000 mL/(g·h), temperature = 60 °C.

of Mn^{4+} to Mn^{3+} and then to Mn^{2+}, while the later peak (β) at more than 420 ℃ was related to the surface reduction of capping oxygen in lattice or the reduction of the bulk metal oxide [38,39]. Compared with pure sludge (S), the H_2 consumption amount significantly increased with the addition of $KMnO_4$ (Table 2). However, not all of the oxygen took part into the redox reaction; instead, the oxygen species that reacted with H_2 at temperatures below 420 °C were related to catalytic performance. This was reflected in the low temperature reducibility and the consumption of surface adsorbed oxygen species [38,40]. As shown in Table 2, the α peak H_2 consumption amount decreased in the sequence of S-MnO_x-1.2 > S-MnO_x-2.4 > S-MnO_x-0.6 > S, indicating that S-MnO_x-1.2 exhibited the strongest low-temperature reducibility and had a higher concentration of active oxygen species. Furthermore, S-MnO_x-1.2 showed the reduction peak at the lowest temperature (383 ℃), suggesting that the surface adsorbed oxygen species on S-MnO_x-1.2 were highly reducible and reactive, which was in good agreement with the O 1*s* results. The strongest low-temperature reducibility, abundance of active oxygen species, and enhanced oxygen mobility of S-MnO_x-1.2 were all favorable for ozone removal.

O_2-TPD was then employed to investigate the evolution of oxygen (Fig. S7). Initially, adsorbed oxygen species and surface active oxygen species (O_2^- and O^-) were desorbed below 400 ℃, followed by the desorption of surface lattice oxygen (O_{latt}) in the range of 400 − 600 °C, and ultimately bulk O_{latt} at temperatures exceeding 600 °C [41]. It is generally reported that a lower temperature of adsorbed oxygen species and surface active oxygen species released, indicating a higher desorption ability of oxygen species on oxygen vacancies [26]. As depicted in Table 2, the S-MnO_x-1.2 exhibited the lowest desorption temperature, suggesting that this catalyst had the strongest desorption ability and mobility of oxygen species, which contributed to its excellent ozone decomposition performance [25].

3.3. Mechanism study

In situ DRIFTs spectra was carried out to elucidate the key information about the ozone decomposition pathway over S-MnO_x-1.2. The assignment of the IR bands corresponding to the various intermediates on the surface of S-MnO_x-1.2 was summarized in Table S4. Under a dry condition (Fig. 5(a, b)), three obvious peaks at 1354 cm^{-1}, ~1330 cm^{-1} and 1220 cm^{-1} were observed, which were related to atomic oxygen intermediates. In contrast, the intensities of superoxide species (O_2^-, 790 cm^{-1}), peroxide species (O_2^{2-}, 940 cm^{-1}) and physical adsorption ozone ($O_{3(ads)}$, 1037 cm^{-1}) were weak [33,42]. These results indicated that ozone decomposed rapidly according to an oxygen vacancy (V_O)-involved mechanism, as illustrated in steps (1)–(3) [7,43].

$$O_{3(ads)} + V_O \rightarrow [O^- \text{-} V_O] + O_2 \tag{1}$$

$$O_3 + [O^- \text{-} V_O] \rightarrow [O_2^{-/2-} \text{-} V_O] + O_2 \tag{2}$$

$$[O_2^{-/2-} \text{-} V_O] \rightarrow V_O + O_2 \tag{3}$$

At first, O_3 molecule adsorbed on the oxygen vacancies over S-MnO_x-1.2, subsequently releasing O_2 molecules and leaving atomic oxygen intermediates on the catalyst surface (Step 1). Atomic oxygen intermediates then reacted with additional O_3 molecules to generate superoxide (O_2^-) or peroxide species (O_2^{2-}) along with the release of O_2 molecules (Step 2). During the ozone removal reaction on the S-MnO_x-1.2 surface, O_2^- or O_2^{2-} rapidly decomposed into O_2 molecule, finally resulting in the recovery of oxygen vacancies (Step 3).

Compared with dry condition, the peak intensity assigned to atomic oxygen intermediate (1354 cm^{-1}, ~1330 cm^{-1} and 1220 cm^{-1}) increased after the addition of H_2O, indicating that the atomic oxygen intermediate was accumulated on the catalyst surface without consumption (Fig. 5(c, d)). Additional O_3 molecules were inhibited to react with the atomic oxygen intermediate due to the competitive adsorption of water vapor (step 2). Therefore, the above result suggested that steps (1)–(3) still occurred during the ozone elimination process over S-MnO_x-1.2 in the humid stream, but these steps were limited by water vapor.

To better understand the mechanism of ozone elimination under the influence of water vapor, the dynamic change of the DRIFT spectra in a flow of O_3 over the water pre-exposed catalyst was recorded (Fig. 6(a)). Upon exposure to water, a broad peak attributed to the stretching vibration of hydroxyl groups (-OH) in the range of 3000–3600 cm^{-1} and the bending mode of adsorbed water at 1633 cm^{-1} became evident [18, 42,44]. After passing O_3 over the water-pretreated catalyst, the bands at 3053 cm^{-1}, 3464 cm^{-1}, 3580 cm^{-1} corresponding to hydroxyl groups and adsorbed water (1633 cm^{-1}) experienced decrease in intensities and eventually vanished. These results indicated that water would adsorb and integrate with surface oxygen vacancies, and ozone would improve [H_2O-V_O] to undergo a chain reaction, resulting in the formation of surface V_O-HO_2^- (Steps 4–8). Under the influence of electron and ozone, the V_O-HO_2^- was rapidly converted into Vo-O_2^{2-} (Steps 9–10). The intensity of O_2^{2-} (940 cm^{-1}) changed negligibly, suggesting that Vo-O_2^{2-} decomposed rapidly into O_2 and achieved the regeneration of oxygen vacancy (Step 11). The surface free hydroxyl (HO•) generated during the decomposition process could interact with oxygen vacancies to form [V_O-OH] (Step 12), which would further participate in the ozone elimination reaction [18,19,33].

$$V_O + H_2O \rightarrow H_2O\text{-}V_O \tag{4}$$

$$H_2O\text{-}V_O + O_3 \rightarrow O_3\text{-}H_2O\text{-}V_O \tag{5}$$

$$O_3\text{-}H_2O\text{-}V_O \rightarrow V_O\text{-}OH + O_2 + HO\bullet \tag{6}$$

$$V_O\text{-}OH + O_3 \rightarrow V_O\text{-}OH\text{-}O_3 \tag{7}$$

$$V_O\text{-}OH\text{-}O_3 + e^- \rightarrow V_O\text{-}HO_2^- + O_2 \tag{8}$$

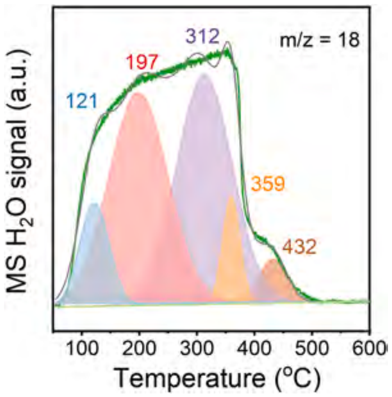

Fig. 7. H_2O-TPD-MS profiles of S-MnO_x-1.2.

$$V_O\text{-}HO_2^- + O_3 \rightarrow V_O\text{-}HO_2^-\text{-}O_3 \quad (9)$$

$$V_O\text{-}HO_2^-\text{-}O_3 + e^- \rightarrow V_O\text{-}O_2^{2-} + O_2 + HO\bullet \quad (10)$$

$$V_O\text{-}O_2^{2-} \rightarrow V_O + O_2 + 2e^- \quad (11)$$

$$V_O + HO\bullet \rightarrow V_O\text{-}OH \quad (12)$$

It is noted in Fig. 6(a) that the peaks assigned to atomic oxygen intermediate (1354 cm^{-1}, ~1330 cm^{-1} and 1220 cm^{-1}) appeared after feeding gaseous O_3 over water pre-exposed catalyst. This phenomenon demonstrated again that steps (1)–(3) took part in the ozone elimination process over S-MnO_x-1.2 in the humid stream. A transient experiment under alternating humidity conditions was conducted (Fig. 6(b)). The ozone conversion gradually declined when S-MnO_x-1.2 was exposed to 10 vol% H_2O. The activity could be restored to a higher level after switching to dry gas. However, with repeated introduction of water vapor, ozone conversion rapidly dropped to the level of the previous cycle and continued to decrease. After four cycles, the activity finally decreased to 63% of ozone conversion under humid condition. These results indicated that the negative effect of water vapor had accumulated, leading to the consumption and reduction in the number of oxygen vacancies for ozone decomposition [19,25].

However, as shown in Fig. 6(b), the ozone removal activity did not decrease dramatically over time due to the consumption of oxygen vacancies; instead, it eventually stabilized at approximately 58% after a 48-hour continuous test at 10 vol% H_2O. This phenomenon suggested that some of the oxygen vacancies would not suffer from water and still be active for ozone elimination. If there were only one type of oxygen vacancy, excess water vapor would cover the oxygen vacancies and prevent O_3 from being adsorbed on the active sites, leading to the deactivation of catalyst and even causing ozone conversion to drop to zero when all oxygen vacancies were poisoned by water. However, due to the presence of other types of oxygen vacancies, which still have the ability to decompose ozone in excess water vapor condition, resulting in ~60% of ozone conversion after 48 h. Therefore, there were two types of oxygen vacancies on the S-MnO_x-1.2 surface for ozone decomposition, some of which were denoted as ozone-friendly, and some of which were denoted as hydrophilic [7,25,42]. Ozone-friendly oxygen vacancies were responsible for adsorbing O_3 and catalyzing ozone decomposition, but their activities were easily restrained by water vapor. On the contrary, hydrophilic oxygen vacancies preferred to occupy with H_2O and form [V_O-OH] for ozone elimination.

It is noteworthy that β-MnOOH is a 2D layered structure filled with interlayer hydroxyl groups (-OH) [37]·H_2O-TPD was conducted to gain a deeper understanding of the H_2O adsorption on the catalyst surface (Fig. 7). The water desorption peaks observed at 121 ℃ and 197 ℃ were attributed to physically adsorbed water, while the peak at 312 ℃ was ascribed to chemically adsorbed water [9,33,45]. It can be seen that the S-MnO_x-1.2 catalyst possessed 49.5% of physically adsorbed water and 40.9% of chemically adsorbed water (Table S5). This result implied that a larger amount of water molecules could be physiosorbed on the surface hydroxyl groups of the S-MnO_x-1.2 catalyst through weak hydrogen-bonding interactions. This, in turn, hindered the chemisorption of water and a great number of ozone-friendly oxygen vacancies were protected from water vapor poisoning. The presence of hydrophilic oxygen vacancies, coupled with the reduced susceptibility to water poisoning in ozone-friendly oxygen vacancies, all of which were responsible for the outstanding ozone removal performance and superior H_2O durability of the S-MnO_x-1.2 catalyst.

Based on the above experimental results, the probable mechanism of ozone decomposition under humid condition over sludge-derived S-MnO_x-1.2 catalyst was summarized in Scheme 1. Two possible routes involving oxygen vacancies were identified. Route I: hydrophilic oxygen vacancies were occupied by H_2O to form V_O-OH and V_O-OH_2^-, which

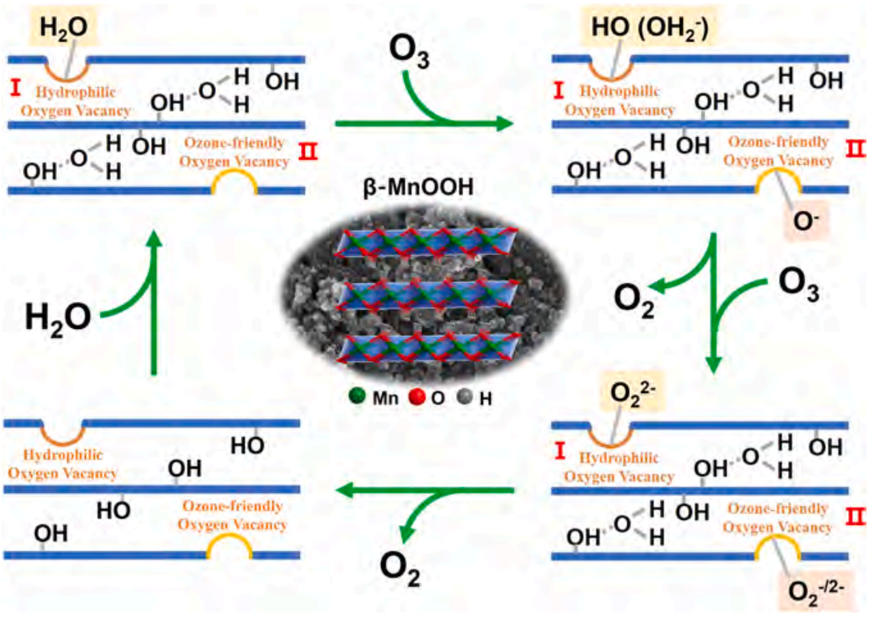

Scheme 1. The probable mechanism of ozone decomposition under humid condition over sludge-derived S-MnO_x-1.2 catalyst.

then reacted with ozone to produce O_2. Route II: ozone reacted with ozone-friendly oxygen vacancies to generate O_2. Upon completion of these two routes, the oxygen vacancies and the catalyst would achieve regeneration and get ready for the next cycle of the reaction. The presence of surface hydroxyl groups could physically adsorb abundant water molecules and thus improve the water resistance of S-MnO_x-1.2 catalyst.

4. Conclusion

$KMnO_4$ treatment was effective for sludge disintegration. In this study, $KMnO_4$ also acted as a chemical modifier to incorporate Mn oxides and contribute to the synthesis of Mn oxide-doped catalysts. The obtained S-MnO_x-1.2 catalyst could efficiently remove gaseous ozone under 5 vol% H_2O condition within the industrial flue gas temperature range of 40 to 80 ℃. The excellent ozone removal performance can be attributed to its large surface area, plentiful oxygen vacancies and interlayer hydroxyl groups. Oxygen vacancy-involved mechanism played a crucial role in the ozone decomposition process. Hydroxyl groups from β-MnOOH physically adsorbed abundant water molecules, hindered water chemically adsorbed on ozone-friendly oxygen vacancies, and thus improved the water resistance of S-MnO_x-1.2 catalyst. Our research not only provides a promising catalyst to control the industrial ozone pollution, but also promotes the high value-added utilization of waste sludge.

CRediT authorship contribution statement

Lyumeng Ye: Conceptualization, Methodology, Validation, Data curation, Formal analysis, Investigation, Writing - Original Draft, Writing - review & editing. **Wenjing Dai:** Methodology, Writing - review & editing. **Peng Lu:** Resources, Data curation, Writing - review & editing, Funding acquisition, Project administration. **Jianhang Huang:** Validation, Data curation. **Xianhui Yan:** Validation, Formal analysis, Investigation. **Changcheng Sun:** Investigation. **Kuang He:** Investigation. **Mingyang Zhang:** Investigation. **Haibao Huang:** Methodology, Resources, Writing - review & editing, Supervision, Funding acquisition.

Declaration of Competing Interest

The authors declare that they have no known competing financial interests or personal relationships that could have appeared to influence the work reported in this paper.

Data Availability

The authors do not have permission to share data.

Acknowledgments

This work was supported by the National Key Research and Development Plan of China (2022YFC3701705), the Guangdong Basic and Applied Basic Research Foundation (2022A1515110085), the Project of Science and Technology Program of Guangzhou (2024A04J4989), the Central Public-interest Scientific Institution Basal Research Fund of China (PM-zx703-202305-202, PM-zx703-202305-176), and Zhongshan Social Welfare and Basic Research Project (200827093620848).

Appendix A. Supporting information

Supplementary data associated with this article can be found in the online version at doi:10.1016/j.apcatb.2024.123696.

References

[1] L. Ye, X. Wang, S. Fan, W. Chen, M. Chang, S. Zhou, Z. Wu, Q. Fan, Photochemical indicators of ozone sensitivity: application in the Pearl River Delta, China, Front. Environ. Sci. Engin 10 (2016) 49–62.
[2] H. Liu, S. Liu, B. Xue, Z. Lv, Z. Meng, X. Yang, T. Xue, Q. Yu, K. He, Ground-level ozone pollution and its health impacts in China, Atmos. Environ. 173 (2018) 223–230.
[3] A. Gaudel, A step forward to mitigate ozone, Nat. Geosci. 15 (2022) 513–514.
[4] A. Li, Q. Zhou, Q. Xu, Prospects for ozone pollution control in China: an epidemiological perspective, Environ. Pollut. 285 (2021) 117670.
[5] D. Ding, J. Xing, S. Wang, Z. Dong, F. Zhang, S. Liu, J. Hao, Optimization of a NO_x and VOC cooperative control strategy based on clean air benefits, Environ. Sci. Technol. 56 (2022) 739–749.
[6] P. Lu, L. Ye, X. Yan, J. Huang, P. Zhao, Z. Tang, D. Chen, C. Cen, Unraveling the impact of SO_2 on electron transfer and oxygen vacancy over MnO_x-CeO_2 for ozone decomposition, Sep Purif. Technol. 333 (2024) 125909.
[7] X. Li, J. Ma, H. He, Recent advances in catalytic decomposition of ozone, J. Environ. Sci. 94 (2020) 14–31.
[8] M. Namdari, C.-S. Lee, F. Haghighat, Active ozone removal technologies for a safe indoor environment: a comprehensive review, Build. Environ. 187 (2021) 107370.
[9] G. Zhu, W. Zhu, Y. Lou, J. Ma, W. Yao, R. Zong, Y. Zhu, Encapsulate α-MnO_2 nanofiber within graphene layer to tune surface electronic structure for efficient ozone decomposition, Nat. Commun. 12 (2021) 4152.
[10] R. Fang, H. Huang, J. Ji, M. He, Q. Feng, Y. Zhan, D.Y.C. Leung, Efficient MnO_x supported on coconut shell activated carbon for catalytic oxidation of indoor formaldehyde at room temperature, Chem. Eng. J. 334 (2018) 2050–2057.
[11] D.W. Kwon, G.J. Kim, J.M. Won, S.C. Hong, Influence of Mn valence state and characteristic of TiO_2 on the performance of Mn–Ti catalysts in ozone decomposition, Environ. Technol. 38 (2017) 2785–2792.
[12] W. Dai, B. Zhang, J. Ji, B. Liu, R. Xie, Y. Gan, X. Xie, J. Zhang, P. Huang, H. Huang, Exceptional ozone decomposition over δ-MnO_2/AC under an entire humidity environment, Environ. Sci. Technol. 57 (2023) 17727–17736.
[13] J.A. Bennett, K. Wilson, A.F. Lee, Catalytic applications of waste derived materials, J. Mater. Chem. A 4 (2016) 3617–3637.
[14] M.M. Mian, N. Alam, M.S. Ahommed, Z. He, Y. Ni, Emerging applications of sludge biochar-based catalysts for environmental remediation and energy storage: A review, J. Clean. Prod. 360 (2022) 132131.
[15] L. Kou, J. Wang, L. Zhao, K. Jiang, X. Xu, Coupling of $KMnO_4$-assisted sludge dewatering and pyrolysis to prepare Mn,Fe-codoped biochar catalysts for peroxymonosulfate-induced elimination of phenolic pollutants, Chem. Eng. J. 411 (2021) 128459.
[16] X. Zhang, H. Cai, J. Shen, H. Zhang, Effects of potassium permanganate conditioning on dewatering and rheological behavior of pulping activated sludge: mechanism and feasibility, RSC Adv. 8 (2018) 41172–41180.
[17] C. Wu, G. Zhang, P. Zhang, C.-C. Chang, Disintegration of excess activated sludge with potassium permanganate: Feasibility, mechanisms and parameter optimization, Chem. Eng. J. 240 (2014) 420–425.
[18] H. Tang, Z. Wang, J. Shao, F. Lin, P. Liu, Y. He, Y. Zhu, Catalytic decomposition of residual ozone over cactus-like MnO_2 nanosphere: synergistic mechanism and SO_2/H_2O interference, ACS Omega 7 (2022) 9818–9833.
[19] G. Zhu, J. Zhu, W. Jiang, Z. Zhang, J. Wang, Y. Zhu, Q. Zhang, Surface oxygen vacancy induced α-MnO_2 nanofiber for highly efficient ozone elimination, Appl. Catal., B 209 (2017) 729–737.
[20] J. Ma, X. Li, C. Zhang, Q. Ma, H. He, Novel $CeMn_aO_x$ catalyst for highly efficient catalytic decomposition of ozone, Appl. Catal., B 264 (2020) 118498.
[21] M.M. Mian, G. Liu, B. Fu, Y. Song, Facile synthesis of sludge-derived MnO_x-N-biochar as an efficient catalyst for peroxymonosulfate activation, Appl. Catal., B 255 (2019) 117765.
[22] Y. Li, B. Zou, C. Hu, M. Cao, Nitrogen-doped porous carbon nanofiber webs for efficient CO_2 capture and conversion, Carbon 99 (2016) 79–89.
[23] M. Shabanian, M. Hajibeygi, A. Raeisi, FTIR characterization of layered double hydroxides and modified layered double hydroxides, in: S. Thomas, S. Daniel (Eds.), Layered Double Hydroxide Polymer Nanocomposites, 2, Woodhead Publishing, 2020, pp. 77–101.
[24] S. Xiong, J. Chen, N. Huang, T. Yan, Y. Peng, J. Li, The poisoning mechanism of gaseous HCl on low-temperature SCR catalysts: MnO_x-CeO_2 as an example, Appl. Catal., B 267 (2020) 118668.
[25] X. Li, J. Ma, L. Yang, G. He, C. Zhang, R. Zhang, H. He, Oxygen vacancies induced by transition metal doping in γ-MnO_2 for highly efficient ozone decomposition, Environ. Sci. Technol. 52 (2018) 12685–12696.
[26] W. Hong, J. Ma, T. Zhu, H. He, H. Wang, Y. Sun, F. Shen, X. Li, To enhance water resistance for catalytic ozone decomposition by fabricating H_2O adsorption-site in OMS-2 tunnels, Appl. Catal., B 297 (2021) 120466.
[27] J. Yang, S. Hu, L. Shi, S. Hoang, W. Yang, Y. Fang, Z. Liang, C. Pan, Y. Zhu, L. Li, J. Wu, J. Hu, Y. Guo, Oxygen vacancies and Lewis acid sites synergistically promoted catalytic methane combustion over perovskite oxides, Environ. Sci. Technol. 55 (2021) 9243–9254.
[28] L. Ye, P. Lu, Y. Xianhui, H. Huang, Boosting simultaneous catalytic removal of NO_x and toluene via cooperation of Lewis acid and oxygen vacancies, Appl. Catal., B 331 (2023) 122696.
[29] J. Ma, C. Wang, H. He, Transition metal doped cryptomelane-type manganese oxide catalysts for ozone decomposition, Appl. Catal., B 201 (2017) 503–510.
[30] J. Jia, P. Zhang, L. Chen, Catalytic decomposition of gaseous ozone over manganese dioxides with different crystal structures, Appl. Catal., B 189 (2016) 210–218.

[31] C. Dong, Z. Qu, X. Jiang, Y. Ren, Tuning oxygen vacancy concentration of MnO_2 through metal doping for improved toluene oxidation, J. Hazard. Mater. 391 (2020) 122181.

[32] W. Yang, Za Su, Z. Xu, W. Yang, Y. Peng, J. Li, Comparative study of α-, β-, γ-and δ-MnO_2 on toluene oxidation: oxygen vacancies and reaction intermediates, Appl. Catal., B 260 (2020) 118150.

[33] B. Zhang, J. Ji, B. Liu, D. Zhang, S. Liu, H. Huang, Highly efficient ozone decomposition against harsh environments over long-term stable amorphous MnO_x catalysts, Appl. Catal., B 315 (2022) 121552.

[34] M. Wang, P. Zhang, J. Li, C. Jiang, The effects of Mn loading on the structure and ozone decomposition activity of MnO_x supported on activated carbon, Chinese, J. Catal. 35 (2014) 335–341.

[35] D. Chlala, J.-M. Giraudon, M. Labaki, J.-F. Lamonier, Formaldehyde total oxidation on manganese-doped hydroxyapatite: the effect of Mn content, Catalysts (2020).

[36] C. Jiang, P. Zhang, B. Zhang, J. Li, M. Wang, Facile synthesis of activated carbon-supported porous manganese oxide via in situ reduction of permanganate for ozone decomposition, Ozone.: Sci. Eng. 35 (2013) 308–315.

[37] B. Liu, Y. Sun, L. Liu, S. Xu, X. Yan, Advances in manganese-based oxides cathodic electrocatalysts for Li–air batteries, Adv. Funct. Mater. 28 (2018) 1704973.

[38] J. Chen, X. Chen, X. Chen, W. Xu, Z. Xu, H. Jia, J. Chen, Homogeneous introduction of CeO_y into MnO_x-based catalyst for oxidation of aromatic VOCs, Appl. Catal., B 224 (2018) 825–835.

[39] L. Liu, B. Wang, X. Yao, L. Yang, W. Jiang, X. Jiang, Highly efficient MnO_x/biochar catalysts obtained by air oxidation for low-temperature NH_3-SCR of NO, Fuel 283 (2021) 119336.

[40] F. Liu, S. Rong, P. Zhang, L. Gao, One-step synthesis of nanocarbon-decorated MnO_2 with superior activity for indoor formaldehyde removal at room temperature, Appl. Catal., B 235 (2018) 158–167.

[41] J. Yang, S. Hu, Y. Fang, S. Hoang, L. Li, W. Yang, Z. Liang, J. Wu, J. Hu, W. Xiao, C. Pan, Z. Luo, J. Ding, L. Zhang, Y. Guo, Oxygen vacancy promoted O_2 activation over perovskite oxide for low-temperature CO oxidation, ACS Catal. 9 (2019) 9751–9763.

[42] Z. Xu, W. Yang, W. Si, J. Chen, Y. Peng, J. Li, A novel γ-like MnO_2 catalyst for ozone decomposition in high humidity conditions, J. Hazard. Mater. 420 (2021) 126641.

[43] R. Cao, P. Zhang, Y. Liu, X. Zheng, Ammonium-treated birnessite-type MnO_2 to increase oxygen vacancies and surface acidity for stably decomposing ozone in humid condition, Appl. Surf. Sci. 495 (2019) 143607.

[44] Y. Liu, W. Yao, X. Cao, X. Weng, Y. Wang, H. Wang, Z. Wu, Supercritical water syntheses of Ce_xTiO_2 nano-catalysts with a strong metal-support interaction for selective catalytic reduction of NO with NH_3, Appl. Catal., B 160-161 (2014) 684–691.

[45] X. Zhang, F. Bi, Z. Zhu, Y. Yang, S. Zhao, J. Chen, X. Lv, Y. Wang, J. Xu, N. Liu, The promoting effect of H_2O on rod-like $MnCeO_x$ derived from MOFs for toluene oxidation: a combined experimental and theoretical investigation, Appl. Catal., B 297 (2021) 120393.